

Design and Modelling of Electrical Impedance Tomography-based 3D-Printed Patterned Soft Tactile skins

Author 1¹, Author 2², Author 3³, Author 4³ Author 5¹

Abstract—The ability to estimate contact information is becoming increasingly relevant for robotic applications. Consequently, there is a growing need for technologies that can provide dense and distributed contact information in a compact form factor. This work presents the design and modeling of a thin-form-factor tactile skin based on electrical impedance tomography measurements. This technology enables the creation of tactile skins of arbitrary size without requiring any embedded electronic components. We demonstrate how patterning these 3D-printed skins can improve the accuracy and precision of contact localization and force estimation. A comprehensive framework for the automatic fabrication and calibration of tactile skins is presented, paving the way for customizable soft tactile skins.

I. INTRODUCTION

In order to perceive and interact with the world around us, humans have highly developed tactile sensing systems, with sensitivity distributions varying with location on our skins [1], [2]. In order to provide robotic systems with equivalent levels of information, the area of soft and flexible ‘e-skins’ aims to create sensorized surfaces and membranes which can be applied onto existing actuated systems and soft substrates, such as a robotic arm or hand [3]. To approach capabilities comparable to those of humans, these skins must be able to detect and localize small tactile stimuli over large areas, while being highly manufacturable: thin, flexible, robust, and reliable.

The majority of a hand’s tactile interactions involve the fingertips, where signals are complex and spatiotemporally distributed [4], [5]. Introducing sensors at this scale is therefore of particular interest in soft robotics: fingertip-scale solutions include force sensitive resistors [6], which provide quantitative measurements with a very limited number of channels, and embedded fibers ([7], [8]), which can be manufactured with more custom morphologies but which risk delamination during high strains. Additionally, a number of approaches exist which use the entire bulk of the fingertip to contain the sensor: vision-based tactile sensors such as the DIGIT [9], [10]; barometric chambers [11], which can be distributed over entire volumes and 3D printed in place [12], and hall effect sensors, which can be morphologically ‘programmed’ at small scales [13].

Electrical impedance tomography (EIT) has been introduced as a method of localizing tactile stimuli on resistively-responsive e-skins [14]–[17], with benefits including a significant number of channels from few electrodes, the ability to position electrodes at the skin’s perimeter, and the potential

for multimodal sensing capabilities [18]. However, when homogeneous and isotropic materials are used, the sensitivity of the skins deteriorates with distance from electrodes. Multi-layer solutions can be introduced to minimize this effect [19], or anisotropic patterns can be used to bias the voltage fields generated over the skins by an applied current. For example, by combining two piezoresistive materials, Costa Cornellà et al. demonstrated how multi-layered patterned anisotropic surfaces could be used to customize the sensitivity distributions of EIT-based skins. In particular, a pattern of radial spokes was shown to increase sensitivity at the centre of a 110 mm diameter circular skin [20]. However, these patterns were limited to only two layers, and their manual fabrication technique limited this approach from being miniaturized to fingertip-scale implementations.

In this work, we explore how similarly patterned surfaces can be fabricated at the fingertip-scale, employing a more versatile fabrication method: pellet-based 3D printing with resolutions of 0.1 mm. Using this approach, we physically compare five rectangular patterns, finding radial designs to provide the best localization capabilities over the 30.5 × 22.9 mm area. Based on this finding, we expand beyond [20]’s two-layered designs, fabricating and analyzing four-layered patterns, which we find to achieve 53.2% improvement in position prediction accuracy (from 7.58 mm to 3.55 mm). In doing so, we focus on the ways in which changes to the material, fabrication, and morphology of the conductive skins themselves can be used to customize their raw output signals, which can then be fed into sophisticated EIT reconstruction algorithms. In this case, we use feedforward neural networks as a tool to directly compare the information contained within the raw signals of different sensor morphologies/patterns, such that we can understand the key design principles required to scale our approach up to implementation in complex-shaped robotic fingertips, hands, and bodies.

II. METHODOLOGY AND DESIGN

A. EIT-based Sensing Principle

EIT is a non-invasive imaging technique that reconstructs the internal conductivity distribution of a conductive body through boundary electrical potential measurements. When applied to a thin, soft, and stretchable conductive layer whose internal resistance responds to its physical deformation, this technique creates an effective tactile sensing system [14]. In the EIT-based skin system, a known current is injected through a pair of electrodes (source and sink) and voltage measured across another pair of electrodes. This current generates an electrical potential distribution u across the

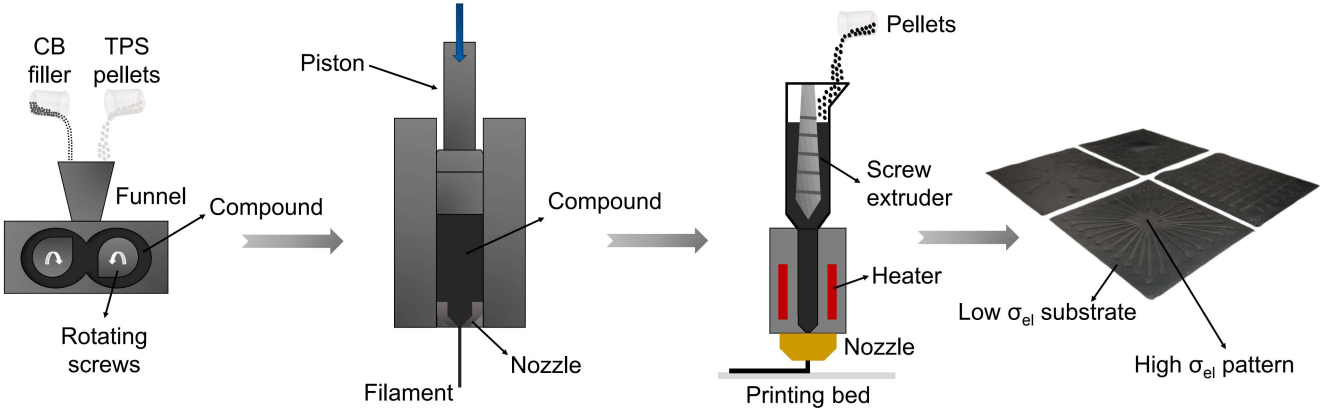


Fig. 1. Schematic of the conductive skin fabrication process, including compounding, extruding, 3D printing, and four different patterned skins.

conductive body Ω . The relationship between the potential distribution u and the body's internal impedance distribution σ is governed by the equation:

$$\nabla \cdot (\sigma \cdot \nabla u) = 0 \quad \text{in } \Omega \quad (1)$$

When external forces are applied to the skin, its internal impedance distribution σ changes as a function of contact information: position (\mathbf{x}, \mathbf{y}) and force magnitude \mathbf{F} . The voltage measurements u from the remaining electrodes can be used to reconstruct this impedance distribution by solving the nonlinear inverse problem. By using the learning-based methods, this inverse problem can be formulated as a mapping function between the electrical measurements and contact information:

$$u = f(\sigma(\mathbf{x}, \mathbf{y}, \mathbf{F})) \quad (2)$$

where $f(\sigma(\cdot))$ represents the nonlinear relationship that can be learned through data-driven methods.

A complete measurement cycle requires using all electrode combinations for current injection and voltage measurement. There are two main injection modes: adjacent and opposite [21]. In the adjacent mode, two injection electrodes are next to each other, while in the opposite mode, two injection electrodes are separated by half electrodes. The choice affects the measurement count per driving pair. For n electrodes skin, there are $(n - 3)$ measurements for the adjacent mode and $(n - 4)$ measurements for the opposite mode. This work employed opposite current injections and adjacent measurements.

B. Skin Fabrication and Pattern Print

In this study, the conductive skins were produced through Fused Deposition Modeling (FDM) 3D printing [22]. Thermoplastic styrene block copolymer (TPS) composites with carbon black (CB) were chosen for their combination of flexibility, piezoresistive properties, and suitability for FDM (fused deposition modeling) fabrication method, as demonstrated in earlier research [23] [24]. To create the composite materials, the elastomer matrix and CB filler were combined in a HAAKE Polylab Rheomix 600 torque rheometer (ThermoFisher, Karlsruhe, Germany). After heating up to 175 °C,

the TPS elastomer (TF2ATL, Kraiburg TPE, Waldkraiburg, Germany) and ENSACO 260G CB filler (Timcal, Bodio, Switzerland) were blended for 30 minutes at 30 rpm (Table I). Due to friction from the mixing process, the temperature rose to around 190 °C. In the following step, the compounded materials were transferred into an RH7 capillary rheometer (NETZSCH, Selb, Germany) and extruded into filaments at 190 °C with a nozzle diameter of 1.75 mm and an extrusion speed of 5 mm/min.

TABLE I
TPS/CB COMPOUNDS EXAMINED IN THIS RESEARCH

Parameters	Compounds	
Matrix	TF2ATL	
Matrix Shore Hardness (A)	22	
Matrix density (g/cm ³)	0.88	
CB amount (wt.%)	20	40
Compound Shore Hardness (A)	48	76
Resistivity (Ohm · m)	14.817	0.009

TABLE II
3D PRINTING PARAMETERS USED TO PRODUCE THE CONDUCTIVE SKINS

	TF2ATL (20 wt. % CB)	TF2ATL (40 wt. % CB)
Nozzle diameter (mm)	0.4	0.4
Layer height (mm)	0.1	0.1
Extrusion width (mm)	0.4	0.4
Input Temp. (°C)	125	150
Output Temp. (°C)	205	205
Extrusion Multiplier	3.5	3.5
Print speed (mm/s)	25	15

The 1.75 mm filaments from each compound were cut into 2-3 mm long pellets and then loaded into a commercial screw extruder 3D printing head (Tumaker Pro Dual, Tumaker, Valencia, Spain). Simplify3D software was used for slicing and generating the required G-codes to print the conductive skins. A nozzle of 0.4 mm and a layer height of 0.1 mm were selected to achieve high precision. The temperatures, extrusion multiplier, and printing speeds are provided in (Table II). The skin structures, measuring 44 mm x 35 mm, were printed using the printer's multi-material functionality. A 0.1 mm thick base layer of low-conductive material was first printed with one print head, followed by a 0.1 mm

high-conductive pattern applied with the second print head. Four patterns were printed in the later study. The fabrication process, from compounding to extrusion and ultimately 3D printing, and skin samples are illustrated in Fig. 1.

III. PATTERN DESIGN OPTIMIZATION STUDY

A. Experimental Setup

As shown in Fig. 2, an experimental platform with multiple components was developed to facilitate automated data collection for tactile sensing evaluation. The experimental platform was based on a modified commercial 3D printer (Creality Ender-3 Pro), which enables precise positioning control with the capability of 0.1 mm resolution. A force sensor (Sparkfun TAL220 Series Parallel Beam Load Cell) equipped with a 1.4 mm diameter probe, was attached to the printer head for controlled force application on the skin surface. The force measurements were processed through an Arduino Uno microcontroller via the amplifier (SparkFun Load Cell Amplifier - HX711). The tactile skin was placed on a custom base that was securely mounted on the printer's platform. To provide proper pressure measurement conditions, the skin's bottom surface was supported by a silicon substrate (Smooth-On Ecoflex 00-30), while its electrode-patterned side faced upward and was contacted by 32 circular electrodes arranged in a rectangular pattern on a custom PCB (Fig. 2). Each electrode had a diameter of 2 mm, with a pitch of 4 mm between electrodes. The PCB was connected to an open source EIT board [25] for signal acquisition, which was performed using alternating current injection at a frequency of 10 kHz.

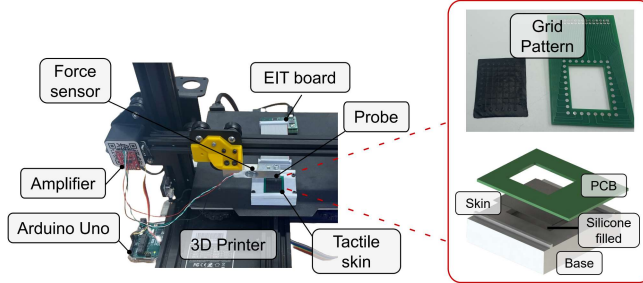


Fig. 2. Experimental setup showing the tactile skin pressed by a modified 3-axis platform equipped with a force sensor. Key components include the EIT board and Arduino Uno for data collection. The skin is fixed on the platform and its patterned electrodes are aligned with the PCB.

B. Data Collection

The data collection process involved EIT signal collection, probe positioning, force measurement and their data synchronization. The objective of the data collection is to gather comprehensive tactile skin's response to various pressure stimuli on its surface. The EIT board kept reading the signal through the USB connection to PC. The EIT signals were collected at a frequency of 1.3 Hz and each measurement was timestamped for subsequent synchronization. The printer control thread executed a four-state cycle for each measurement point.

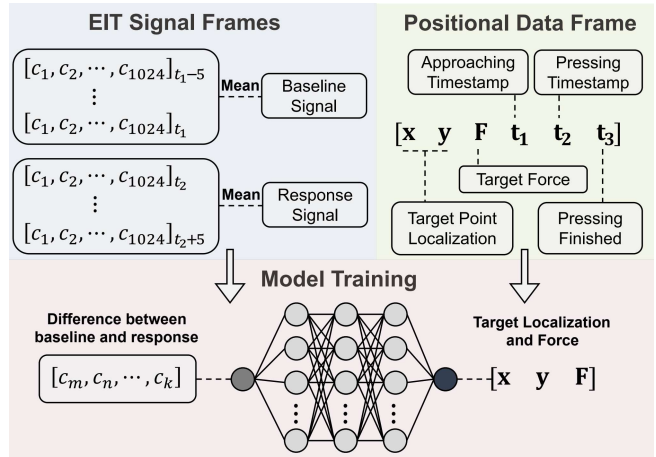


Fig. 3. Data processing pipeline for the neural network training.

- Move: A random coordinate (x, y) is generated within the skin's sensing area. The printer then positions the probe precisely above this location.
- Press: For a specified target force F , the printer head descends vertically in precise 0.2 mm increments. At each step, the force reading thread monitors the applied force until reaching the target value.
- Hold: While achieving the target force, the probe maintains its position for 5 seconds. This ensures stable pressure on the skin and allows the skin to reach a steady-state response.
- Release: The probe retracts from the skin surface, completing one measurement cycle.

This automated procedure was executed across thousands of points for each skin pattern to ensure comprehensive spatial coverage and statistical reliability.

C. Data Process and Neural Network Training

The data processing pipeline is shown in Fig. 3. The aim of this process was to align the EIT data with positional and force data. The EIT measurements were acquired continuously at 1.3 Hz, with each frame containing 1024 voltage measurements. After removing zero-value readings, 896 effective voltage measurements remain for each frame. The positional data contains the target point coordinates (x, y) , target force magnitude F , and three timestamps: the approach initiation t_1 , the moment of achieving target force t_2 , and the probe retraction t_3 . For each measurement point, the skin's response was computed by comparing two temporal windows of EIT signals: a baseline signal averaged from five consecutive frames before probe contact (t_1), and a response signal averaged from five frames during the force holding period (t_2). The final input feature vector was the difference between these two averaged signals, effectively isolating the deformation-induced changes in conductivity distribution as well as reducing signal temporal noise.

The neural network architecture consists of an input layer with the 896 processed voltage features, followed by three fully connected hidden layers with 200, 100, and 30 nodes respectively, and a 3-node regression output layer predicting

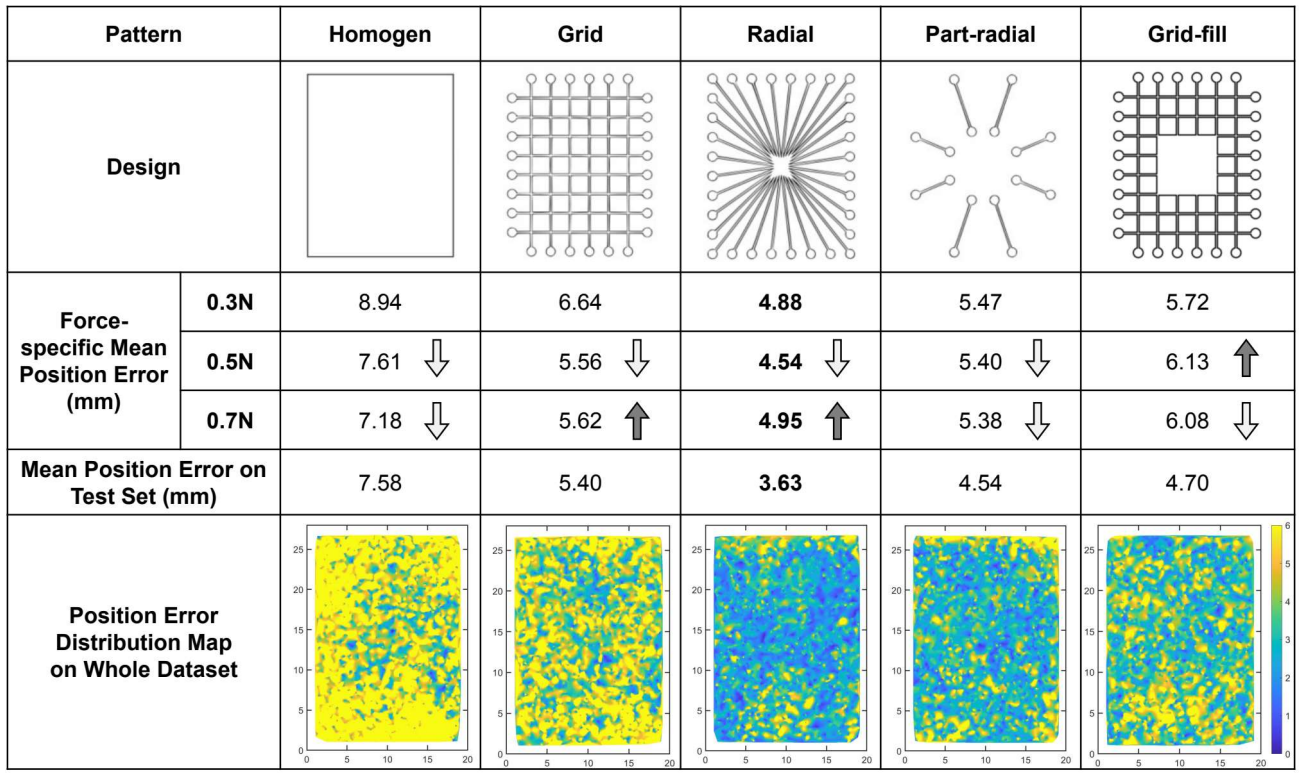


Fig. 4. Comparison of five electrode pattern designs and their sensing prediction performances. These patterns were printed on one side of the skin. The numbers present the mean position errors between the predicted contact position and the ground truth, with arrows indicating performance trend between force levels. The error distribution maps across all sensing area are with color scale indicating error magnitude from 0 mm (blue) to 6 mm (yellow).

position (\mathbf{x}, \mathbf{y}) and force \mathbf{F} . To prevent overfitting, a dropout layer with a rate of 0.2 was implemented before the second hidden layer. This network architecture was applied across all skin patterns' evaluations, whether training on force-specific datasets or the complete force range dataset. All the input data were split into training, validation and test (80%, 10%, 10%) sets. The network was trained using stochastic gradient descent with momentum, initialized with a learning rate of 0.003 and mini-batches of size 1024. Early stopping was applied to prevent overfitting.

D. Pattern Comparison Results

One homogeneous and four structured electrode patterns were evaluated to identify the optimal pattern design for the tactile skin. Fig. 4 presents five designs alongside their performance metrics, including force-specific position prediction errors, overall position errors, and spatial error distribution maps. This evaluation methodology focused on pattern comparison rather than achieving optimal network performance. For each pattern, 3000 data points (1000 measurements at each force level: 0.3 N, 0.5 N, and 0.7 N) were collected. To ensure a fair comparison, the same neural network architecture and training parameters were used across all patterns, with each dataset split into training (80%), validation (10%), and test (10%) sets. The mean position error results are all based on the test set.

1) *Force-Specific Pattern Performance:* By comparing the prediction errors of the five pattern designs, the radial pattern demonstrated superior performance than other designs across

all force levels. The Radial pattern consistently performed better than other configurations, achieving the lowest mean position errors for all force levels. While the Homogen pattern showed the poorest performance, its error decreased notably with increasing force (from 8.94 mm at 0.3 N to 7.18 mm at 0.7 N), suggesting that larger deformations generate more distinctive electrical signatures on this pattern. Other structured patterns (Grid, Part-radial, and Grid-fill) showed intermediate performance, indicating that organized electrode arrangements generally improved sensing capability compared to the Homogen configuration. Thus, the spatial organization of electrodes played a crucial role in the skin's ability to detect and localize pressure points.

2) *Pattern Design Analysis:* The overall performance metrics (combining all 3000 points on three force levels) highlighted that the Radial pattern has the best performance (3.63 mm), which can be attributed to its geometric properties. It is believed that the Radial pattern's symmetrical arrangement and its balanced electrode density across the sensing area contribute to its superior performance. The position error distribution maps revealed that all electrode patterns face challenges in edge regions, suggesting an inherent limitation in the current single-layer design approach.

The results revealed that electrode geometry configuration on the skin significantly influences its sensing accuracy, with the Radial pattern demonstrating the best performance in position prediction. However, there are still limitations across all patterns: reduced accuracy in edge regions and poor force sensitivity in our prior tests. These limitations suggested that

while electrode pattern optimization can enhance position sensing, the single-layer skin structure might have inherent constraints in capturing the full range of contact information. Based on these findings, we selected the Radial pattern as our foundation for further development, hypothesizing that a multi-layer structure could address these limitations. The multi-layer approach was motivated by the potential for enhanced pressure sensitivity, as multiple deformable layers could create more pronounced changes in conductivity distribution under applied force [19]. This structural modification aimed to improve both position accuracy and force prediction capabilities by generating more distinctive electrical signatures across the sensing range.

IV. MULTI-LAYER SKIN

A. Multi-layer Skin Design and Fabrication

To enhance the accuracy of position and force sensing in the sensor skin, a new approach was developed involving a multi-layered skin design with electrode-patterned surfaces on both sides. In this design, the electrode patterns were mirrored and alternated so that half of the electrodes were positioned on each side. Additionally, to improve the signal-to-noise ratio, the thickness of the patterned layers was increased from 0.1 mm to 0.2 mm. The multi-layered structure was produced by printing each half separately in direct contact with the printing bed. After printing, the two halves were peeled off and aligned on top of each other. Finally, the layers were physically bonded by laminating the assembled skin in an oven at 180 °C under a 5 kg weight for 60 minutes (Fig. 5).

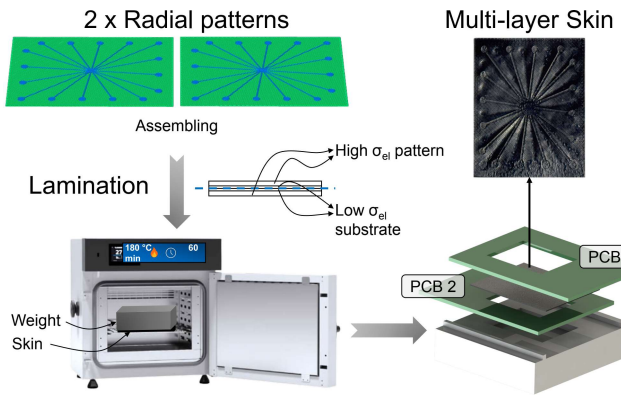


Fig. 5. Assembling and lamination of multi-layer skins. The completed multi-layer skin is mounted in between two PCBs for electrical connections.

B. Comparative Performance Analysis

To evaluate the effectiveness of the multi-layer design, a comprehensive comparison study was conducted between single and multi-layer configurations, both using the Radial pattern. The dataset comprised 4000 random press points for each configuration, with applied forces ranging from 0.3 N to 1.3 N. The data was split into training (80%), validation (10%), and test (10%) sets. To ensure a fair comparison, identical neural network architecture and training parameters were maintained across both configurations. Table III shows

the performance metrics on the test set. The multi-layer configuration achieved substantial improvement in position prediction, reducing the mean position error by 24.6% from 4.71 mm to 3.55 mm. This result proved that the multi-layered structure enhanced the sensitivity of the skin and provided more distinct electrical signatures for different pressure locations than single-layered skin. Compared with the previous force-specific experiments, the single-layer Radial pattern skin's higher position error might be attributed to the additional noise introduced by random force applications across a wider range (0.3-1.3 N). While the multi-layer structure highly enhanced the contact position prediction, the improvement in force prediction was tiny, with only a marginal decrease in mean error from 0.24 N to 0.23 N.

TABLE III
PERFORMANCE ANALYSIS OF SINGLE AND MULTI-LAYER
RADIAL PATTERN CONFIGURATIONS

Performance Metric	Skin Structure	
	Single-layered	Multi-layered
Mean Position Error (mm)	4.71	3.55
Mean Force Error (N)	0.24	0.23

C. Force Range-Specific Analysis

To further understand the prediction behavior of the multi-layer skin, we analyzed both position and force prediction errors across five force ranges from 0.3 N to 1.3 N, and the results are shown in Fig. 6. The position prediction demonstrated relatively consistent performance across all force ranges, with errors varying by only 0.51 mm between the highest (3.85 mm at 0.3-0.5 N) and lowest (3.34 mm at 0.7-0.9 N) points. This stability in position prediction suggests that the multi-layer structure maintains consistent spatial sensitivity across varying contact forces. In contrast, the force prediction accuracy shows marked dependence on the applied force range. The error decreases substantially from 0.33 N in the lowest range (0.3-0.5 N) to 0.19 N in the intermediate range (0.5-0.7 N), then the error further

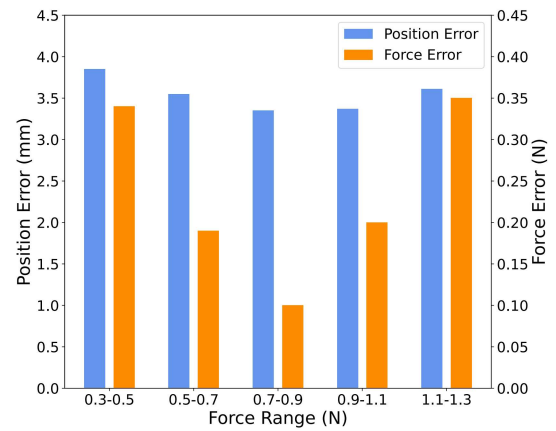


Fig. 6. Analysis of position and force prediction errors across different force ranges for the multi-layer tactile skin.

decreases to 0.10 N in the 0.7-0.9 N range, achieving a total error reduction of 69.7% from the initial range. This behavior might be attributed to several reasons: The neural network tended to optimize predictions toward the median force values. The skin's thinness (0.6 mm) limited its force sensitivity. Besides, the material characteristics of the skin were crucial. While increasing force should theoretically generate more distinctive signals, excessive forces might push the elastic material beyond its optimal deformation range, leading to either saturation of the response or potential plastic deformation that compromises signal uniqueness.

V. CONCLUSION AND DISCUSSION

This work presents a comprehensive framework for designing and fabricating EIT-based patterned tactile skins through high-resolution 3D printing technology, with thicknesses as small as 0.2 mm. Through systematic evaluation of different electrode patterns, we demonstrated that structured patterns significantly enhance contact position prediction compared to homogeneous configurations, with the Radial pattern achieving the best performance among all designs. The subsequent development of a multi-layer structure further enhanced the skin's sensing capabilities. The multi-layer skin also demonstrated consistent spatial sensitivity across varying contact forces. However, there remain opportunities for improvement in force prediction accuracy. Future work could explore alternative material compositions, pattern designs optimized specifically for force sensing, and more sophisticated multi-layer architectures.

REFERENCES

- [1] R. Ackerley, I. Carlsson, H. Wester, H. Olausson, and H. Backlund Wasling, "Touch perceptions across skin sites: differences between sensitivity, direction discrimination and pleasantness," *Frontiers in Behavioral Neuroscience*, vol. 8, 2014. [Online]. Available: <https://www.frontiersin.org/journals/behavioral-neuroscience/articles/10.3389/fnbeh.2014.00054>
- [2] F. Mancini, A. Bauleo, J. Cole, F. Lui, C. A. Porro, P. Haggard, and G. D. Iannetti, "Whole-body mapping of spatial acuity for pain and touch," *Annals of Neurology*, vol. 75, no. 6, pp. 917–924, 2014. [Online]. Available: <https://onlinelibrary.wiley.com/doi/abs/10.1002/ana.24179>
- [3] W. Wang, Y. Jiang, D. Zhong, Z. Zhang, S. Choudhury, J.-C. Lai, H. Gong, S. Niu, X. Yan, Y. Zheng, C.-C. Shih, R. Ning, Q. Lin, D. Li, Y.-H. Kim, J. Kim, Y.-X. Wang, C. Zhao, C. Xu, X. Ji, Y. Nishio, H. Lyu, J. B.-H. Tok, and Z. Bao, "Neuromorphic sensorimotor loop embodied by monolithically integrated, low-voltage, soft e-skin," *Science*, vol. 380, no. 6646, pp. 735–742, 2023. [Online]. Available: <https://www.science.org/doi/abs/10.1126/science.adc0086>
- [4] T. Nonaka, A. Abdulali, C. Sirithunge, K. Gilday, and F. Iida, "Soft robotic tactile perception of softer objects based on learning of spatiotemporal pressure patterns," in *2023 IEEE International Conference on Soft Robotics (RoboSoft)*, 2023, pp. 1–7.
- [5] M. Mete, H. Jeong, W. D. Wang, and J. Paik, "Sori: A softness-rendering interface to unravel the nature of softness perception," *Proceedings of the National Academy of Sciences*, vol. 121, no. 13, p. e2314901121, 2024. [Online]. Available: <https://www.pnas.org/doi/abs/10.1073/pnas.2314901121>
- [6] A. Ke, J. Huang, L. Chen, Z. Gao, J. Han, C. Wang, J. Zhou, and J. He, "Fingertip tactile sensor with single sensing element based on fsr and pvd," *IEEE Sensors Journal*, vol. 19, no. 23, pp. 11 100–11 112, 2019.
- [7] J. Hughes and F. Iida, "Tactile sensing applied to the universal gripper using conductive thermoplastic elastomer," *Soft Robotics*, vol. 5, no. 5, pp. 512–526, 2018. [Online]. Available: <https://doi.org/10.1089/soro.2017.0089>
- [8] A. Georgopoulou and F. Clemens, "Piezoresistive elastomer-based composite strain sensors and their applications," *ACS Applied Electronic Materials*, vol. 2, no. 7, pp. 1826–1842, 2020. [Online]. Available: <https://doi.org/10.1021/acsaelm.0c00278>
- [9] M. Lambeta, P.-W. Chou, S. Tian, B. Yang, B. Maloon, V. R. Most, D. Stroud, R. Santos, A. Byagowi, G. Kammerer, D. Jayaraman, and R. Calandra, "Digit: A novel design for a low-cost compact high-resolution tactile sensor with application to in-hand manipulation," *IEEE Robotics and Automation Letters*, vol. 5, no. 3, pp. 3838–3845, 2020.
- [10] P. Potdar, D. Hardman, E. Almanzor, and F. Iida, "High-speed tactile braille reading via biomimetic sliding interactions," *IEEE Robotics and Automation Letters*, vol. 9, no. 3, pp. 2614–2621, 2024.
- [11] O. Shorthose, A. Albini, L. He, and P. Maiolino, "Design of a 3d-printed soft robotic hand with integrated distributed tactile sensing," *IEEE Robotics and Automation Letters*, vol. 7, no. 2, pp. 3945–3952, 2022.
- [12] C. Tawk, M. in het Panhuis, G. M. Spinks, and G. Alici, "Soft pneumatic sensing chambers for generic and interactive human-machine interfaces," *Advanced Intelligent Systems*, vol. 1, no. 1, p. 1900002, 2019. [Online]. Available: <https://onlinelibrary.wiley.com/doi/abs/10.1002/aisy.201900002>
- [13] S. Lee and J. Hughes, "Morphological and material programability of a hall-effect based soft tactile sensors," in *2024 IEEE 7th International Conference on Soft Robotics (RoboSoft)*, 2024, pp. 325–331.
- [14] D. Silvera-Tawil, D. Rye, M. Soleimani, and M. Velonaki, "Electrical impedance tomography for artificial sensitive robotic skin: A review," *IEEE Sensors Journal*, vol. 15, no. 4, pp. 2001–2016, 2015.
- [15] K. Park, H. Yuk, M. Yang, J. Cho, H. Lee, and J. Kim, "A biomimetic elastomeric robot skin using electrical impedance and acoustic tomography for tactile sensing," *Science Robotics*, vol. 7, no. 67, p. eabm7187, 2022. [Online]. Available: <https://www.science.org/doi/abs/10.1126/scirobotics.abm7187>
- [16] D. Hardman, T. G. Thuruthel, and F. Iida, "Tactile perception in hydrogel-based robotic skins using data-driven electrical impedance tomography," *Materials Today Electronics*, p. 100032, 2023. [Online]. Available: <https://www.sciencedirect.com/science/article/pii/S2772949423000086>
- [17] T. Zhao, C. Wu, and M. Soleimani, "Ionic liquid based distributed touch sensor using electrical impedance tomography," *IOP SciNotes*, vol. 1, no. 2, p. 025005, sep 2020. [Online]. Available: <https://dx.doi.org/10.1088/2633-1357/abb345>
- [18] M. Abdelwahed, L. Zerioul, A. Pitti, and O. Romain, "Using novel multi-frequency analysis methods to retrieve material and temperature information in tactile sensing areas," *Sensors*, vol. 22, no. 22, 2022. [Online]. Available: <https://www.mdpi.com/1424-8220/22/22/8876>
- [19] Y. Wang, D. Naritomi, H. Shigemune, and T. G. Thuruthel, "Multi-layer electrical impedance tomography based soft tactile skins," in *2024 IEEE 7th International Conference on Soft Robotics (RoboSoft)*, 2024, pp. 1101–1106.
- [20] A. Costa Cornellà, D. Hardman, L. Costi, J. Brancart, G. Van Assche, and F. Iida, "Variable sensitivity multimaterial robotic e-skin combining electronic and ionic conductivity using electrical impedance tomography," *Scientific Reports*, vol. 13, no. 1, p. 20004, Nov 2023. [Online]. Available: <https://doi.org/10.1038/s41598-023-47036-5>
- [21] B. Liu, B. Yang, C. Xu, J. Xia, M. Dai, Z. Ji, F. You, X. Dong, X. Shi, and F. Fu, "pyeit: A python based framework for electrical impedance tomography," *SoftwareX*, vol. 7, pp. 304–308, 2018.
- [22] C. Bascucci, J. Hughes, and F. Clemens, "3d printable piezoresistive skin-like tactile sensors for soft robotics," 2024.
- [23] A. Georgopoulou, T. Sebastian, and F. Clemens, "Thermoplastic elastomer composite filaments for strain sensing applications extruded with a fused deposition modelling 3d printer," *Flexible and Printed Electronics*, vol. 5, no. 3, p. 035002, 2020.
- [24] A. Georgopoulou, B. Vanderborght, and F. Clemens, "Multi-material 3d printing of thermoplastic elastomers for development of soft robotic structures with integrated sensor elements," in *Industrializing Additive Manufacturing: Proceedings of AMPA2020*. Springer, 2021, pp. 67–81.
- [25] J. Zhu, J. C. Snowden, J. Verdejo, E. Chen, P. Zhang, H. Ghaednia, J. H. Schwab, and S. Mueller, "EIT-kit: An Electrical Impedance Tomography Toolkit for Health and Motion Sensing," in *UIST 2021 - Proceedings of the 34th Annual ACM Symposium on User Interface Software and Technology*. Association for Computing Machinery, Inc, 10 2021, pp. 400–413.